Effect of rear-fuselage design on the aerodynamics of a helicopter at side-slip angle

Drew Gingras[a], Felix Weis[b], Bryan Godbolt[c], Sina Ghaemi[a,*]

[a] *Department of Mechanical Engineering, University of Alberta, Edmonton, Alberta, T6G 1H9, Canada*

[b] *University of Stuttgart, Stuttgart, Baden-Württemberg, 70174, Germany*

[c] *QinetiQ Target Systems Canada, Medicine Hat, Alberta, Canada*

The aerodynamic design of a helicopter fuselage encounters many complexities that arise from the large variation in side-slip angle during different flight maneuvers and gusty conditions. A wind tunnel investigation was performed on a scaled-down helicopter model at Reynolds number of $Re_w = 9.6\times10^5$ to analyze its aerodynamic performance up to a 40° side-slip angle. Four rear-fuselage configurations were investigated including a removable motor geometry, as well as a cusped and a round enclosure for the motor. A six-axis load cell was used to determine three components of force and moment acting on the fuselage. Planar PIV measurements were performed in the fuselage wake to analyze effect of side-slip angle (β) and rear-fuselage on the wake flow. The drag force coefficients displayed a parabolic increase with rising β. The pitch moment strongly depended on the aft-body design. The cusped rear-body had the largest pitch moment (C_m) at zero-side slip while the round case had the smallest magnitude. For all the rear-fuselage configurations, the slope of the pitching moment ($dC_m/d\beta$) changed sign from negative to positive at $\beta = 20°$. The largest change in $dC_m/d\beta$ was observed for the baseline case while the round enclose had the smallest change in $dC_m/d\beta$. The increase in negative C_m with increase of β from zero to 20° was associated with the displacement of the low-pressure core of the wake toward the rear-fuselage. When β increased from 20° to 40°, the wake became skewed and the low-pressure core moved away from the rear-fuselage, causing reduction of the negative C_m toward zero.

Nomenclature

A_{ref} = reference cross-section area

c = fuselage reference length

C_D = drag coefficient

C_L = lift coefficient

C_l = roll moment coefficient

C_m = pitch moment coefficient

D = drag force acting on the fuselage

L = lift force acting on fuselage

l = roll moment acting on fuselage

m = pitch moment acting on fuselage

Re = Reynolds number

U = streamwise velocity component

u = streamwise velocity fluctuation component

$|\boldsymbol{U}|$ = magnitude of velocity vector, $\sqrt{\langle U\rangle^2 + \langle V\rangle^2}$

U_∞ = freestream velocity, m/s

V = spanwise velocity, m/s

v = spanwise velocity fluctuation, m/s

w = fuselage width

x, y, z = coordinates for wind axes

x', y', z' = coordinates for body-fixed axes

α = angle-of-attack

β = side-slip angle

Abbreviations

CFD = computational fluid dynamics

FOV = field of view

PIV = particle image velocimetry

TE = trailing edge

VGs = vortex generators

I. Introduction

Helicopter fuselages are considered to be bluff bodies since the drag is dominated by pressure force rather than viscous forces. Flow separation in the aft section of bluff bodies is frequent and the main cause of pressure drag and results in imbalance, when the body is subject to a side-slip angle. Cross-flow can occur due to variety of flight maneuvers that helicopters undertake, and sporadic wind gusts at lower flight speeds. As a result, the aerodynamic loading can vary affecting the stability of the helicopter.

The majority of wind tunnel investigations on scaled-down helicopter models in the literature are focused on forward flight at zero side-slip angle. Breitsamter et al. [1] investigated design of skid landing gear and surface mounted VGs for drag reduction on a 1:5 model of a helicopter at α = -10° to 10°. Zanotti et al. [2] used load measurements to evaluate the drag of several appendages, and stereoscopic PIV to analyze the velocity in the aft-body region of a scaled-down NH90 helicopter also during forward flight. Le Pape et al. [3] reported the effectiveness of flow control using steady blowing, pulsed, and synthetic jets on a simplified blunt fuselage model without a rotor system for a wide range of angle-of-attack ($-10^o < \alpha < 6^o$). They observed that the optimal flow control depends on α. De Gregorio et al. [4] investigated a 1:3.88 scale NH90 helicopter with motorized main and tail rotor to characterize the flow field and to analyze aerodynamic interaction between the wake of main rotor and the fuselage at $\alpha = -2.5^o$ and 1.9^o.

There are a limited number of studies that have documented the effect of side-slip angle on the aerodynamic loads and wake of helicopter fuselage. Reß et al. [5] investigated the effect of fuselage and landing gear design, mast fairing, and rotor head on the drag, lift, and yawing moments for $-10^o < \alpha < 10^o$ and side-slip angle of $-10^o < \beta < 10^o$. The study noted a quadratic increase of drag and a linear increase of yawing moment with increase of β. Brunello et al. [6] measured force and moment coefficients for $-180^o < \beta < 180^o$ to develop a database for a 1:10 scaled model of an

Australian Defense Force helicopter. Smoke streams were used to visualize the flow at higher side-slip angles. Sweet and Jenkins [7] measured force and moment coefficients associated with several fuselage configurations in a 7×10 foot wind tunnel for $-12^o \leq \alpha \leq 6^o$ and $-9^o \leq \beta \leq 8^o$. Stepanov et al. [8] investigated the parasitic drag associated with landing gear skid design, external fuel tank geometries, tail stabilizers, and overall fuselage geometry using a 1:7 scaled model of a twin engine light ANSAT helicopter for $-10^o < \alpha < 10^o$ and $-18^o < \beta < 18^o$. These investigations provide insight into the effect of components and appendages on the aerodynamics of the helicopter in cross flow. However, the effect of aft-body design, which is important for any bluff-body, requires further investigation.

Brunello et al. [6] compared the three moment coefficients from their CFD simulation at side-slip angles ranging between ±45° with wind tunnel measurements. Significant discrepancies were noted at high β angles. Boniface [9] utilized CFD to optimize the design of VGs installed on the back ramp of a helicopter for drag reduction at $\beta = 5°$. Filippone [10] carried out CFD on the airframe of a conventional helicopter at a full-scale *Re* number of 30×10^6. The estimated forces from CFD agreed with the reference experiment for the cases in which the flow stayed attached to the fuselage at small α and zero β. Divergence from the experimental measurements was noted as a result of the flow separation with increase of β. A recurring problem with many CFD simulations is the divergence from the experimental data at high side-slip angles when flow separates from the body.

The purpose of this investigation is to measure the aerodynamic loads and characterize the wake flow of a generic helicopter model with four aft-body designs at side-slip angles within $0^o \leq \beta \leq 40^o$. To accomplish this, six-axis load cell measurements and four-camera PIV over a large FOV were performed for four aft-body designs: a baseline aft-body configuration, a configuration without the motor protrusion, and two other configurations with streamlined enclosures for the motor.

II. Experimental Setup

A. Helicopter Model

The experiments were performed in the Department of Mechanical Engineering closed-loop wind tunnel facility at the University of Alberta. The wind tunnel has a 2.4 m × 1.2 m rectangular test section. The maximum test-section velocity is 35 m/s, which was used for the experiments. The test section follows a nozzle with contraction ratio of 6.3:1 with turbulence intensity of 0.4% for free-stream velocity of 35 m/s. More details about the wind tunnel are available at Johnson and Kostiuk [11]. The tests were performed at $Re_c = 9.6\times10^5$, based on fuselage length, *c*,

measured from the nose to the aft most section of the fuselage body ($x' = 0$ in Fig 1a.). The fuselage model under investigation was a scaled-model of an ultra-light helicopter, where the tail boom represents 66% of the model length. The blockage of the wind tunnel cross-section is 3, 3.7, 4.7, 5.2, 5.7, 6.2, and 6.6 percent when side-slip is 0, 10, 20, 25, 30, 35, and 40 degrees. The side-slip angle is applied in the larger dimension of the wind tunnel cross-section (i.e., 2.4 m) to minimize the blockage effect. The fuselage was 3D printed out of ABS plastic and underwent a surface finishing process. A Mini45 six-axis load cell (ATI Industrial Automation) was used to measure the three components of forces and moments. The load cell was mounted to the model internally on a 38.1 mm diameter shaft in a ventral configuration, as shown in Fig. 1b. A round shaft was used to maintain a similar flow interference due to the mount and model connection as the side-slip angle was varied. This eliminates the need to apply any correction on the load measurements when side-slip angle is varied. The body-fixed axes is defined by the coordinate system $x'y'z'$, as shown in Fig. 1a and b. The origin of $x'y'z'$ is located at the center of mass of the helicopter, which is slightly lower than the loadcell center. The load cell is situated 29 mm above and 74 mm forward of the center of mass. The moment coefficients were reported with respect to the body-fixed axes due to compatibility with control inputs. The roll and pitch moments were defined about the longitudinal axis (x'), and the lateral axis (y'), respectively. The aerodynamic drag and lift forces were defined with respect to the wind axes (xyz) as shown in Fig. 1a. The side-slip angle (β) is defined as the angle of the body-fixed axes with respect to the wind axes in the xy plane. Positive β shows rotation of the helicopter around z axis toward its starboard, and a positive rolling moment indicates rotation around the x axis while top part of the fuselage rotates toward the starboard. The positive directions of β, C_l, and C_m are indicated with the arrows in figure 1. The load cell has resolution of 0.25 N and 0.005 Nm in measuring forces and moment, respectively. The maximum estimated uncertainty based on three independent measurements for C_D, C_L, C_l, and C_m are 0.05, 0.02, 0.002, and 0.002, respectively. Each independent measurement includes assembly and alignment of the model with respect to the wind tunnel to include installation errors.

Since origin of the load cell axes did not coincide with the center of mass of the full-scale helicopter, an axis transformation was applied. The aerodynamic loads are presented as dimensionless force and moment coefficients. The reference area A_{ref} and length c used to normalize the coefficients is a constant undisclosed value. Load measurements were collected over a two minute period at a sampling rate of 100 Hz for $\beta = 0°$, 10°, 20°, 30°, and 40°, all at an angle-of-attack of $\alpha = 0°$. Adjustment of the side-slip angle was performed using a tilting rotary table with 1/60° precision.

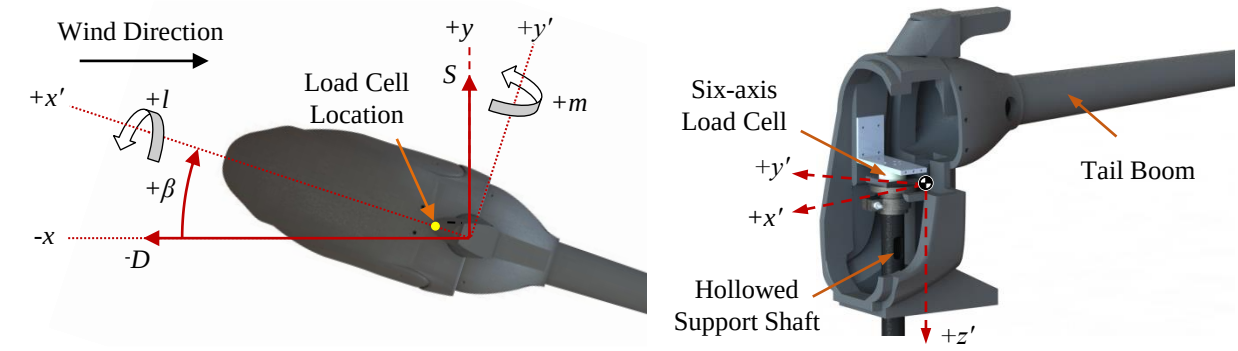

a) b)

Fig. 1 a) Body-fixed axes is represented by *x′y′z′* and the wind axes by *xyz*. Positive direction of the moments are expressed using the right-hand rule. b) Sectioned view showing location of 6-axis load cell, support shaft mount, and the tail-boom.

B. Aft-body Design

Four different aft-body configurations were considered, as outlined in Fig. 2. The baseline configuration in Fig. 2a, has a simplified geometry of the motor at the rear of the fuselage. To test the significance of the motor on aerodynamics at side-slip angles, the fuselage was also tested without the motor, referred to as the empty back configuration, as shown in Fig. 2b. Two additional geometries were also designed to provide an aerodynamic casing around the motor, namely the cusped and round cases shown in Fig. 2c and 2d, respectively.

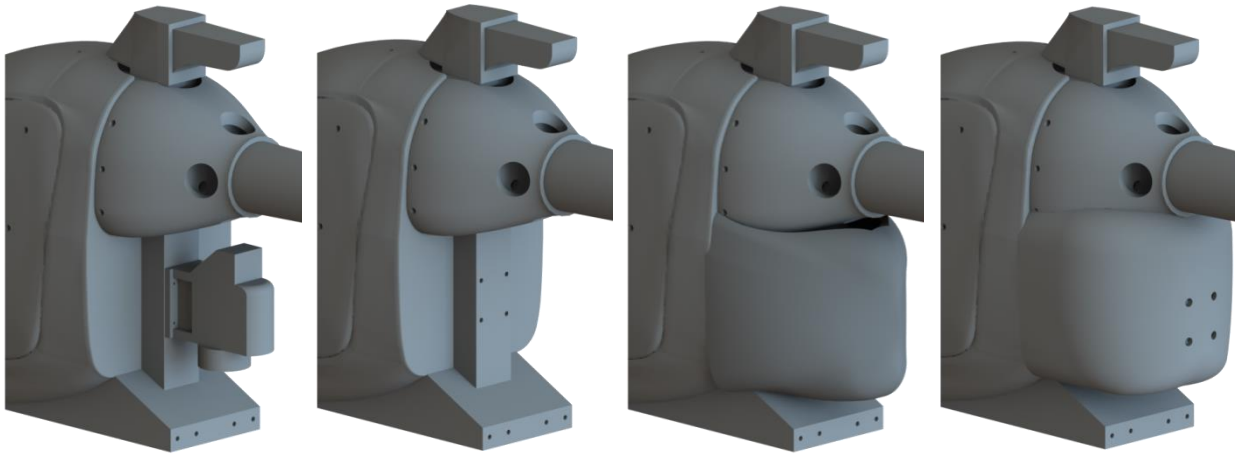

a) b) c) d)

Fig. 2 Aft-body geometries studied in the investigation include a) baseline, b) empty back, c) cusped, and d) round configurations.

C. PIV Setup

Illumination was provided by a dual-cavity Nd:YAG laser (Spectra Physics PIV-400-10) that outputs a 532 nm light beam at 400 mJ per pulse. The light beam was shaped into a laser sheet with 2 mm thickness and ~370 mm width. A fog generator was used to produce water-based tracer droplets with an average diameter of ~2 μm. Four Imager ProX CCD cameras (LaVision GmbH) with a 2048 × 2048 pix sensor were used to capture the FOV. The camera setup shown in Fig. 3 consists of two vertically mounted (number 1 and 2), and two horizontally mounted cameras (number 3 and 4) viewing into 45° angled front-surface mirrors. The horizontally mounted cameras were oriented as such due to space restrictions. Each camera was equipped with a Nikon 50 mm lens with an aperture setting of $f/2$ and digital resolution of 0.092 mm/pix. The imaged region was comprised of four slightly overlapping FOV in the xy plane, each 188 × 188 mm^2 and a combined FOV of 355 × 355 mm^2. The investigated region was located 150 mm above the bottom surface of the fuselage, as shown in Fig 3b, thus the support shaft was considered to have a negligible effect on the PIV measurement domain.

For each measurement, 1000 double-frame images were collected at an average recording rate of 5 Hz. The background noise of the raw images was reduced by subtracting the minimum value of the ensemble images. The data were processed in DaVis 8.3 (LaVision GmbH) using interrogation windows of 96×96 pix (8.8 × 8.8 mm^2) and 75% window overlap. The FOV of the cameras were stitched in DaVis 8.3 using a common coordinate system defined on a custom calibration plate. The uncertainty of PIV is approximately 0.1 pix, as per Raffel et al. [12], which results in velocity uncertainty of about $0.007U_\infty$.

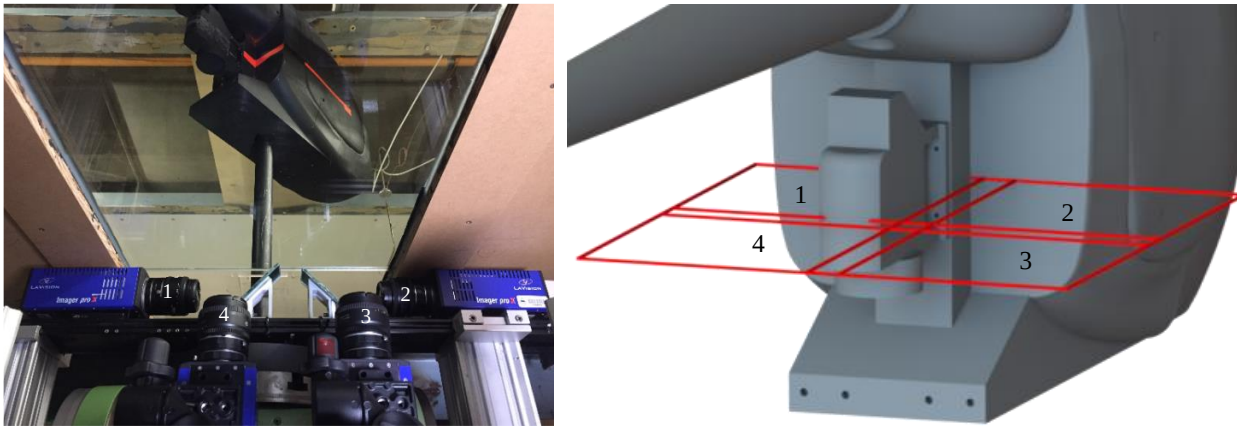

a) b)

Fig. 3 a) Four camera planar PIV setup showing horizontal and vertically mounted cameras. b) Corresponding FOV locations with respect to the fuselage at zero side-slip.

III. Results

A. Load Measurements

The measured drag coefficients of the four aft configurations as well as the drag for a light helicopter model with upsweep rear fuselage at $Re = 3.85\times10^6$ from Stepanov et al. [8] are shown as a function of β in Fig. 4a. Three independent measurements on the baseline configuration were performed to obtain the uncertainty of the measurements. The error bars of the baseline configuration indicate the standard deviation of the data. Since the coefficients presented in Stepanov et al. [8] were multiplied by an undisclosed constant, the values shown in Fig. 5a were scaled to have a relative proximity with the presented data. The overall trend of C_D for all configurations follows a parabolic increase with increasing β. The trend for baseline configuration can be described by a second-order polynomial $C_D = 0.0007\beta^2 + 0.0003\beta + 0.2575$, where β is in degrees.

The C_D of the empty configuration shows minimal difference from the baseline configuration (<5%) over the range of tested β angles. This indicates that the motor section is tucked in a large separation bubble. The cusped case results in up to 20% drag reduction at low side-slip of $\beta \leq 20°$ and a smaller drag reduction of 5% for $20° \leq \beta \leq 30°$, with respect to the baseline configuration. The cusped case reduces the drag due to its streamlined profile. However, for $\beta > 30$, C_D of cusped case increases beyond C_D of the baseline due to flow separation from the trailing-edge tip of the cusped geometry, and its larger cross-section in the freestream direction. The round case was designed to avoid flow separation from the sharp trailing-edge at large β. However, it experiences up to 20% increase in drag at small β with respect to the baseline, and the increment is sustained at larger β. A small convergence of round case towards the baseline is observed for $\beta > 30°$. The larger drag of the round case is associated with a wider recirculation region in its wake as it will be discussed in Section III.B. The lift coefficients in Fig. 4b show that the magnitude of the lift coefficient is up to an order of magnitude smaller than C_D. The small magnitude of C_L and the larger full-scale limit of the loadcell in this z' direction can result in smaller accuracy of this component. However, the three independent measurements proved repeatability of the experiments as seen by the small error bars of the baseline case. There is a significant variation in C_L for $\beta = 0°$; all the configurations result in a negative C_L except the round case. The positive C_L of the round case can be contributed to weaker vortex shedding in the $x'z'$ plane for streamlines passing over the bottom surface of the fuselage. After $\beta = 25°$, the four configurations begin to show larger differences. With the exception of the cusped case, all configurations experience a loss of lift for $\beta > 25°$ that would need to be compensated

by the rotor to maintain a level flight. The cusped case experiences an initial increase of C_L followed by a drop in lift after $\beta = 30°$.

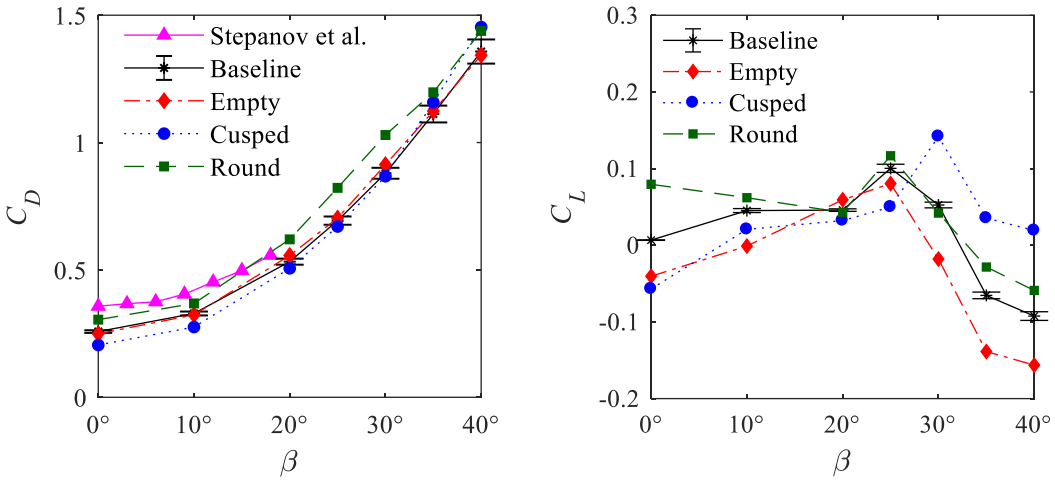

a) **b)**

Fig. 4 Variation of a) drag and b) lift coefficients for the four aft-body configurations with the side-slip angle.

The roll moment coefficient, C_l, in Fig. 5a demonstrates an overall linear growth with β for all configurations. Sweet and Jenkins [7] presented C_l for various helicopter fuselage models with a streamlined aft-body which also showed a linear trend for $-8° \leq \beta \leq 8°$. It is observed that the baseline, cusped, and round geometries have a smaller roll moments compared with the empty configuration for $\beta \leq 25°$. At $\beta \geq 30°$, the roll moment coefficients for the cusped case are notably greater than the other three. The monotonous increase of C_l with β does not pose a significant problem on the stability of the helicopter.

The measured pitch moment coefficients in Fig. 5b have a negative value throughout the β range corresponding to a nose down moment. The cusped case has the largest magnitude while the round case has the smallest C_m at $\beta = 0°$. The values of C_m decrease to larger negative values when β increases to 20° (i.e., $dC_m/d\beta < 0$), where each configuration experiences its maximum nose down pitching moment. The baseline configuration results in a larger negative C_m within $10° \leq \beta \leq 35°$ in comparison to the other configurations. The cusped case, however, has a near-zero slope ($dC_m/d\beta$), and the round case also has a small slope within $0° \leq \beta \leq 20°$ relative to the baseline and empty configurations.

The slope of pitching moments in Fig. 5b has a transition point at $\beta = 20°$, where $dC_m/d\beta$ changes sign from negative to positive. The baseline and empty configurations exhibit a sharp $dC_m/d\beta$ transition at $\beta = 20°$ which can be problematic in flight conditions where crosswinds cause rapid changes in side-slip angle, and consequently, changes the pitching moment. From $\beta = 20°$ to 30°, the cusped and round cases present a reduced $dC_m/d\beta$ by 36% and 67% with respect to the baseline configuration, thus improving the static stability of the vehicle in crosswinds. The measurements show that variation of pitch moment with crossflow strongly depends on the aft-body geometry. This trend is similar to the large variation observed for C_L.

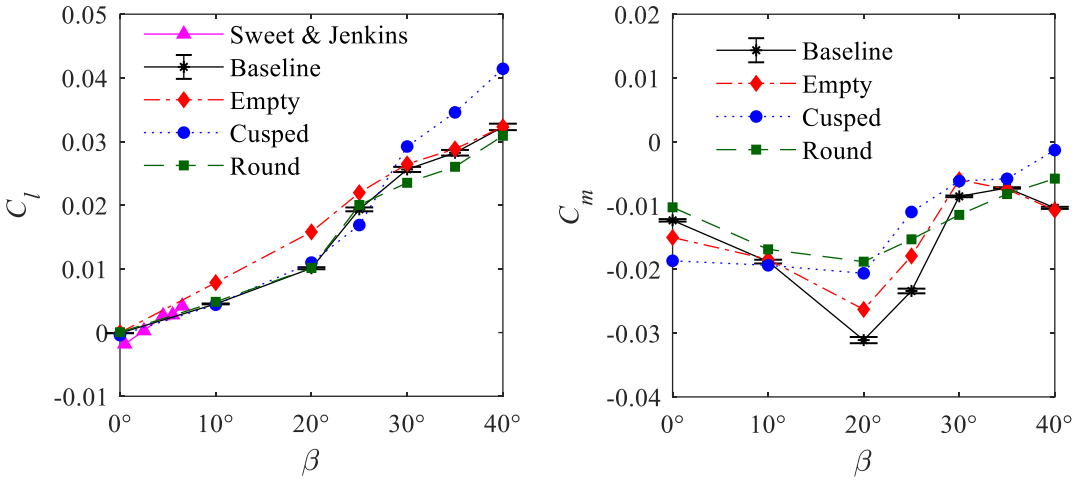

a) **b)**

Fig. 5 Measurment of a) roll and b) pitch moment coefficients for varying side-slip angle.

B. Wake flow

The wake development behind the four different aft-body geometries is investigated without and with crossflow. The normalized magnitude of the mean velocity ($|\boldsymbol{U}|/U_\infty$) in the wake of the fuselage at $\beta = 0$ is shown in Fig. 6a-d. The gray sections in Fig. 6 show the areas in the measurement region where vectors were not computed due to laser sheet blockage or obstruction of the FOV from the lower appendages. The black area shows the cross section of the fuselage geometry at the PIV measurement plane. The white lines indicate contours of zero streamwise velocity (i.e., $U = 0$) to identify the recirculation region of the wake. The dimensions of the FOV are normalized by the length of the fuselage, c.

A large wake deficit is visible in Fig. 6 as a low velocity region with magnitudes less than 20% of U_∞. The flow separation from the fuselage occurs at the sharp corner of the aft-body, $[x/c, y/c] = [0, \pm 0.24]$, in the baseline and empty configurations, as specified in Figs. 6a and 6b. The flow separation for the cusped case in Fig. 6c occurs farther

downstream as a result of the surface curvature. The instantaneous flow separation over the cusped trailing-edge is not bounded to a fixed point and can move along the surface, though the average separation point was found to be [x/c, y/c] = [0.35, ±0.06]. The flow also separates at the beginning of the curvature of the round aft-body at approximately [x/c, y/c] = [0.27, ±0.2] in Fig. 6d. It is also observed that the size of the recirculation region (i.e., separation bubble) for the cusped case is smaller than the three other configurations, as a result of the more streamlined profile. The size of the recirculation region is identified here using the separation point on surface of the aft-section as specified in Fig. 6.

The normalized velocity magnitudes are shown for the baseline fuselage configuration at side-slip angles of β = 10° to 40° in Figs. 7a-d. It is noticed in Fig. 7a that the mean velocity field at β = 10° is skewed slightly in the negative y-direction with respect to the centerline of the fuselage (x' axis) shown with dashed line. As the side-slip angle increases to β = 20° in Fig. 7b, the separation bubble becomes smaller and bulk of the low velocity region in Fig. 7b remains on the negative y side of the fuselage. The smaller wake deficit of β = 20° relative to β = 10°, increases the base pressure, which can contribute to the stronger negative pitch moment of β = 20° in Fig. 5b. With further increase of β, the free-stream also begins to curve the tail of the wake deficit region towards the positive y direction.

The transition between side-slip angles of 20° and 30° provided the largest discrepancy between the load measurements of Figs. 4 and 5. The major difference noticed between the mean velocity fields in Fig. 7b and 7c is that the low velocity bubble concentrates in a smaller region that tilts to the starboard side of the fuselage at β = 20°. The shift of the wake deficit to the starboard side causes the low-pressure region to move away from the aft-body centerline and to project on the starboard side of the aft-body. This resulted in a positive roll moment and a decrease in the pitch moment magnitudes as β is varied from 20° to 30°. As β is further increased to 40° in Fig. 7d, the motor geometry of the baseline configuration clearly protrudes and interferes with the shear-layer separated from the blunt fuselage edge, as shown in Fig. 7d. Additionally, the high β causes the flow to accelerate around the sides of the fuselage, prior to the wake region, as seen by the contours of $|\boldsymbol{U}| / U_\infty > 1$.

The mean velocity fields of the cusped case are shown at side-slip angles of β = 10° to 40° in Figs. 8a-d. The wake begins to displace to the positive y side of the fuselage at β = 30°, as seen in Fig. 8c. The major difference between the wake of the cusped and baseline configurations is that the overall size of the wake deficit and the recirculation region for the cusped case is smaller than the baseline configurations. The smaller wake deficit results in smaller variations in the pitching and rolling moments as the side-slip angle is increased.

The mean velocity fields in the wake of the round case are shown in Fig. 9 for β = 10° to 40°. The round case has a larger and wider wake deficit region than the cusped case, while its wake dimensions are comparable with the baseline. The larger wake deficit exposes a larger aft-body surface to low pressure and results in the larger drag noticed in Fig. 4a. The round case also exhibits a similar accelerated flow region on the sides of the body as the cusped case.

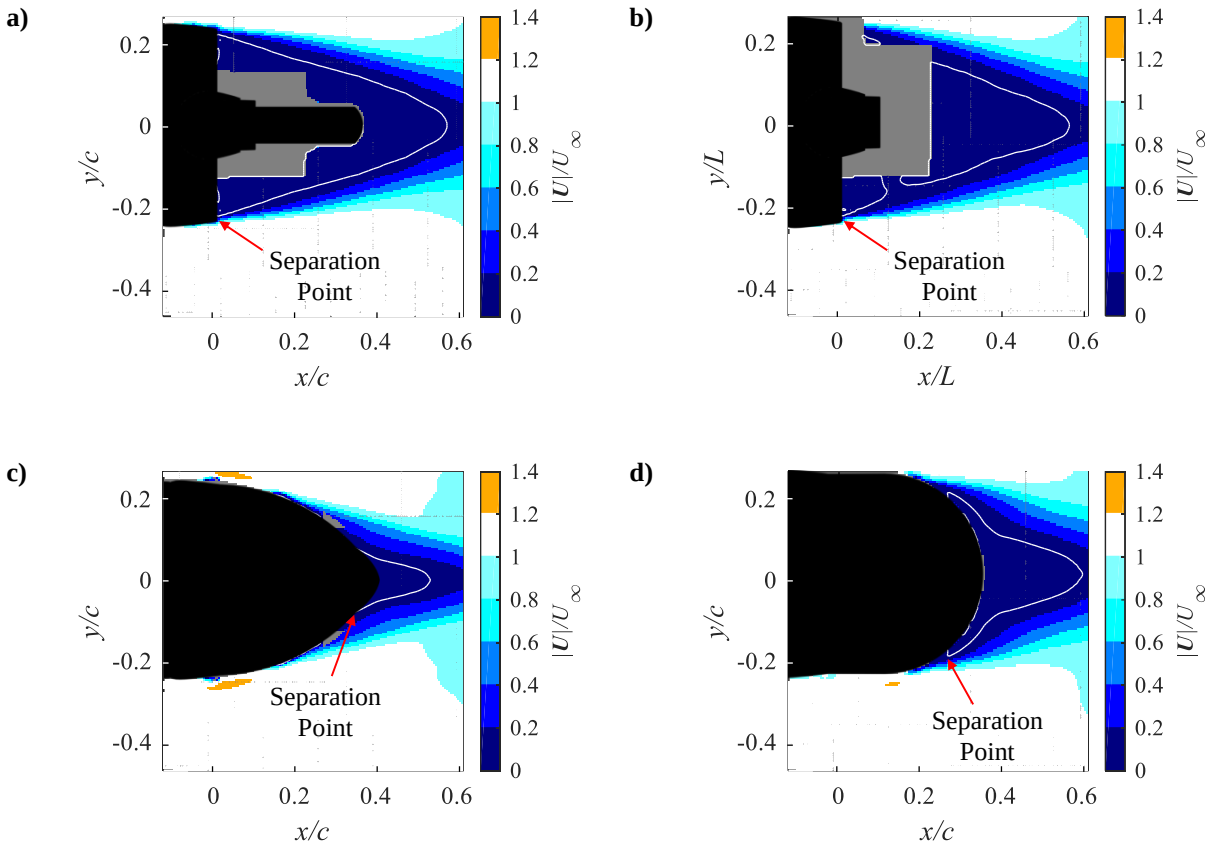

Fig 6. Magnitude of velocity in the wake of a) baseline, b) empty, c) cusped, and d) round case configurations. Zero streamwise velocity is indicated with a white contour to show the boundaries of the recirculation region.

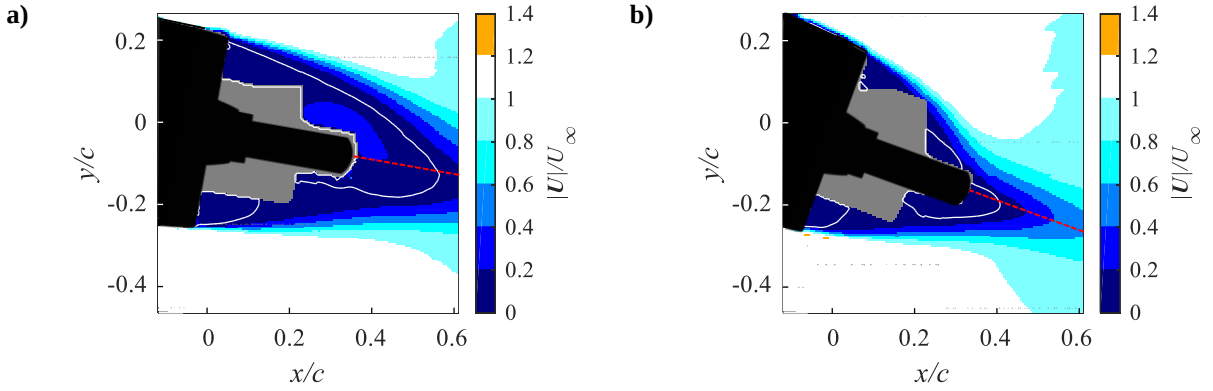

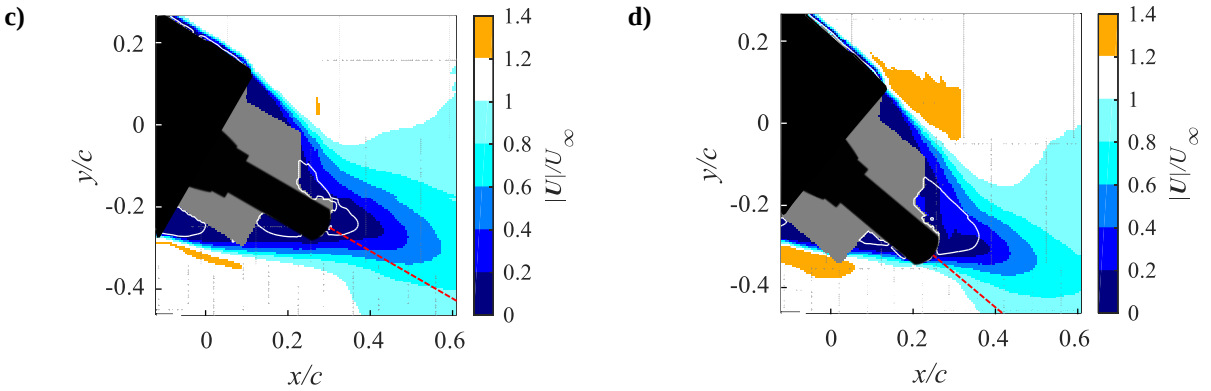

Fig 7. Magnitude of velocity in the wake of the baseline configuration at β of a) 10, b) 20, c) 30, and d) 40°. White contours show zero streamwise velocity.

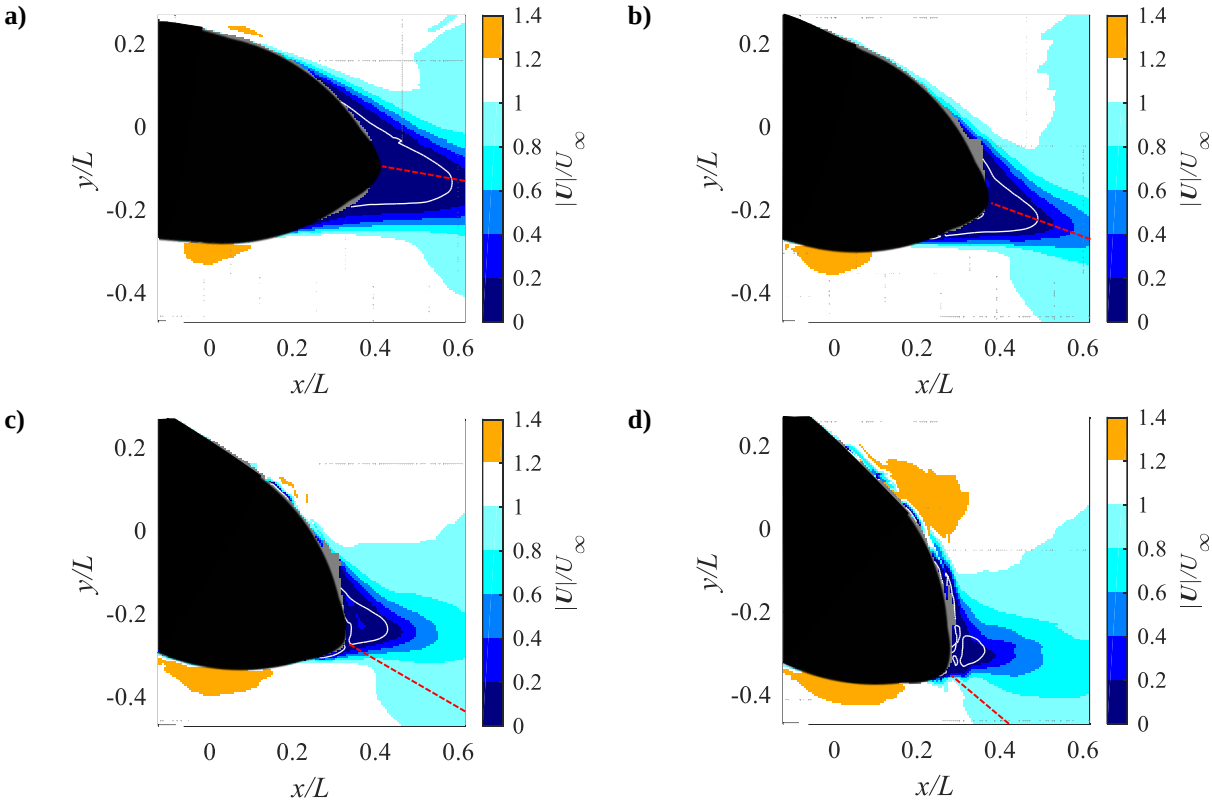

Fig 8. Velocity in the wake of the cusped configuration at β of a) 10, b) 20, c) 30, and d) 40°. White contours show zero streamwise velocity.

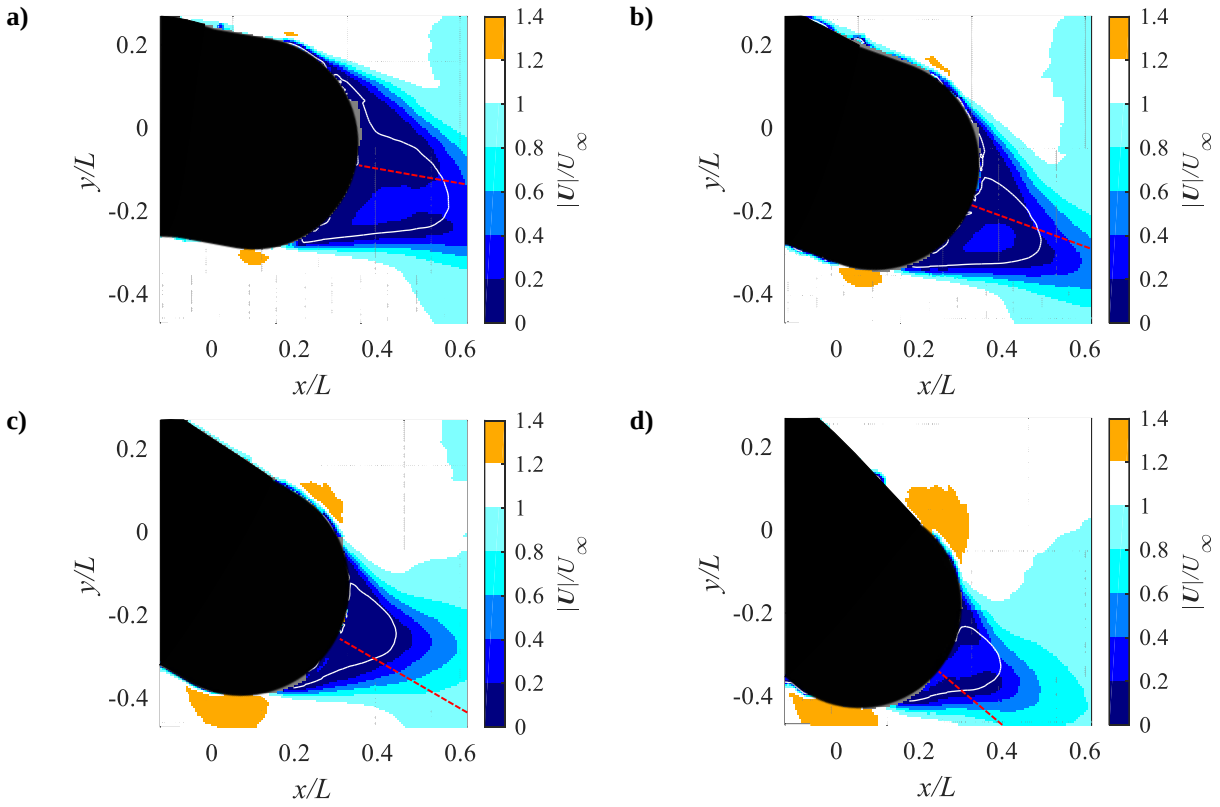

Fig 9. Velocity in the wake of the round case configuration at β of a) 10, b) 20, c) 30, and d) 40 degrees. White contours show zero streamwise velocity.

IV. Conclusions

Six-axis load measurement and particle image velocimetry (PIV) were carried out on a helicopter model with different aft-body geometries to investigate the performance at side-slip angles varying from β = 0° to 40° (nose rotation towards starboard) while angle of attack was kept at zero. The drag force coefficients displayed a parabolic increase with rising β. The cusped case reduced the drag up to 20% for side-slip angles of $\beta \leq 30°$, while the round case increased the drag up to 20% for $0° \leq \beta \leq 40°$, with respect to the baseline configuration. The aft-body design also affected the lift coefficient although the variations were small. At β = 0, a positive lift was only obtained for the round case. Beyond β=30°, the lift coefficient inclined towards larger negative values for all the configuration. The roll moment increased linearly with increasing β. Similar to the lift, the pitch moment also strongly depended on the aft-body design. At β =0, the cusped case had the largest pitch moment while the round case had the smallest magnitude. The pitch moment of the baseline configuration significantly decreased towards larger negative values as β changed from 10° to 20°, and then showed a large increase toward zero between 20° to 30°. This trend was observed for all the aft-bodies; the slope of the pitching moment ($dC_m/d\beta$) changed sign from negative to positive at β = 20°.

However, the cusped case reduced the variation of the pitch moment by 36% relative to the baseline configuration, while the round case reduced the variation by 67%. PIV measurements showed that the separation bubble became smaller by increasing β angle from 0° to 20°. As β increased beyond 20°, PIV measurements showed that the wake became skewed towards the starboard side of the fuselage.

In general, the investigations show that a streamlined aft-body, such as the cusped case, reduces the drag force at small β. An optimized aft-body design similar to the round case, can produce a positive lift coefficient at zero side slip and angle of attack. Both of these factors improve the cruise performance. A streamlined aft-body also smoothens the variation of pitch moment with β, improving the stability of the helicopter in wind gusts with sporadic cross-flow condition.

References

[1] Breitsamter, C., Grawunder, M., and Reß, R., "Aerodynamic Design Optimisation for a Helicopter Configuration Including a Rotating Rotor Head," *29th Congress of the International Aeronautical Council*, St. Petersburg, Russia, 2014

[2] Zanotti, A., *et al.*, "Wind-tunnel Tests of a Heavy-class Helicopter Optimised for Drag Reduction," *The Aeronautical Journal*, Vol. 120, No. 1231, 2016, pp. 1446-1467.

[3] Le Pape, A., Lienard, C., Verbeke, C., Pruvost, M., and De Coninck, J. L., "Helicopter Fuselage Drag Reduction Using Active Flow Control: A Comprehensive Experimental Investigation," *Journal of the American Helicopter Society*, Vol. 60, No. 3, 2015, pp. 1-12.

[4] De Gregorio, F., Pengel, K., and Kindler, K., "A Comprehensive PIV Measurement Campaign on a Fully Equipped Helicopter Model," *Experiments in Fluids*, Vol. 53, No. 1, 2015, pp. 37-49.

[5] Reß, R., Grawunder, M., and Breitsamter, C., "Aerodynamic Analysis of a Helicopter Fuselage with Rotating Rotor Head," *Progress in Flight Physics*, Vol. 7, 2015, pp. 99-110.

[6] Brunello, D., Clarke, G., and Reddy, R.., "Numerical and Experimental Analysis of a Representative ADF Helicopter Fuselage," *28th Congress of the International Aeronautical Council*, Brisbane, Australia, 2012

[7] Sweet, G. E., Jenkins Jr., J. L., "Wind-Tunnel Investigation of the Drag and Static Stability Characteristics of Four Helicopter Fuselage Models," NASA Langley Research Center, Rept. NASA TN D-1363, Hampton, VA, 1962.

[8] Stepanov, R., Zherekhov, V., Pakhov, V., Mikhailov, S., Garipov, A., Yakubov, W., Barakos, G. N., "Experimental Study of Helicopter Fuselage Drag," *Journal of Aircraft*, Vol. 53, No. 5, 2016, pp. 1343-1360.

[9] Boniface, J. C., "A Computational Framework for Helicopter Fuselage Drag Reduction Using Vortex Generators," *Journal of the American Helicopter Society*, Vol. 61, No. 3, 2016, pp. 1-13.

[10] Filippone, A., “Prediction of Aerodynamic Forces on a Helicopter Fuselage,” *The Aeronautical Journal*, Vol. 111, No. 1117, 2007, pp. 175-184.

[11] Johnson, M. R., & Kostiuk, L. W., “Efficiencies of low-momentum jet diffusion flames in crosswind,” Combust. Flame, Vol 123, no. 1, 2000, pp. 189-200.

[12] Raffel, M., Willert, C. C., Scarano, F., Kähler, C. J., Wereley, S. T., Kompenhans, J., “*Particle Image Velocimetry: A Practical Guide*,” 3rd Edition, 2018, Springer, Berlin, Germany.